J. metamorphic Geol., 2008, **26,** 855–870 doi:10.1111/j.1525-1314.2008.00789.x

Oriented growth of garnet by topotactic reactions and epitaxy in high-pressure, mafic garnet granulite formed by dehydration melting of metastable hornblende-gabbronorite (Jijal Complex, Kohistan Complex, north Pakistan)

J. A. PADRÓN-NAVARTA,[1] C. J. GARRIDO,[2] A. SÁNCHEZ-NAVAS,[1,2] A. TOMMASI,[3] V. LÓPEZ SÁNCHEZ-VIZCAÍNO[4], M. T. GÓMEZ-PUGNAIRE[1,2] AND S. S. HUSSAIN[5]

[1]*Departamento de Mineralogía y Petrología, Facultad de Ciencias, Universidad de Granada, 18002 Granada, Spain (padron@ugr.es)*

[2]*Instituto Andaluz de Ciencias de la Tierra (IACT), CSIC, Facultad de Ciencias, 18002 Granada, Spain*

[3]*Géosciences Montpellier, Équipe Manteou-Noyau, CNRS & Université de Montpellier 2, 34095 Montpellier, France*

[4]*Departamento de Geología, Universidad de Jaén, Escuela Politécnica Superior, Alfonso X El Sabio 28, 23700 Linares, Spain*

[5]*Pakistan Museum of Natural History, Garden Avenue, Shakarparian, 44000 Islamabad, Pakistan*

ABSTRACT Garnet growth in high-pressure, mafic garnet granulites formed by dehydration melting of hornblende-gabbronorite protoliths in the Jijal complex (Kohistan palaeo-island arc complex, north Pakistan) was investigated through a microstructural EBSD-SEM and HRTEM study. Composite samples preserve a sharp transition in which the low-pressure precursor is replaced by garnet through a millimetre-sized reaction front. A magmatic foliation in the gabbronorite is defined by mafic-rich layering, with an associated magmatic lineation defined by the shape-preferred orientation (SPO) of mafic clusters composed of orthopyroxene (Opx), clinopyroxene (Cpx), amphibole (Amp) and oxides. The shape of the reaction front is convoluted and oblique to the magmatic layering. Opx, Amp and, to a lesser extent, Cpx show a strong lattice-preferred orientation (LPO) characterized by an alignment of [001] axes parallel to the magmatic lineation in the precursor hornblende-gabbronorite. Product garnet (Grt) also displays a strong LPO. Two of the four ⟨111⟩ axes are within the magmatic foliation plane and the density maximum is subparallel to the precursor magmatic lineation. The crystallographic relationship $\langle 111\rangle_{Grt}//[001]_{Opx,Cpx,Amp}$ deduced from the LPO was confirmed by TEM observations. The sharp and discontinuous modal and compositional variations observed at the reaction front attest to the kinetic inhibition of prograde solid-state reactions predicted by equilibrium-phase diagrams. The *P–T* field for the equilibration of Jijal garnet granulites shows that the reaction affinities are 5–10 kJ mol.$^{-1}$ for the Grt-in reaction and 0–5 kJ mol.$^{-1}$ for the Opx-out reaction. Petrographic and textural observations indicate that garnet first nucleated on amphibole at the rims of mafic clusters; this topotactic replacement resulted in a strong LPO of garnet. Once the amphibole was consumed in the reaction, the parallelism of [001] axes of the mafic-phase reactants favoured the growth of garnet crystals with similar orientations over a pyroxene substrate. These aggregates eventually sintered into single-crystal garnet. In the absence of deformation, the orientation of mafic precursor phases conditioned the nucleation site and the crystallographic orientation of garnet because of topotaxial transformation reactions and homoepitaxial growth of garnet during the formation of high-pressure, mafic garnet-granulite after low-pressure mafic protoliths.

Key words: amphibole dehydration-melting; EBSD; garnet; HP mafic granulite; Jijal complex; Kohistan; topotaxy and epitaxy.

INTRODUCTION

The knowledge of the mechanisms of garnet growth during metamorphic reactions is necessary for estimating the rate of metamorphic reactions and, hence, for using metamorphic textures and metamorphic *P–T–t* paths to unravel tectonic and geodynamic processes. The kinetics of garnet growth and nucleation during metamorphic reactions has been investigated through the analysis of 2D and 3D compositional zoning of garnet, crystal sizes and spatial distribution, by combining X-ray tomography and statistical analysis of the microstructure, numerical modelling of crystal habits and textures, and measurements of lattice-preferred orientation (LPO) of precursor phases and garnet by electron backscatter diffraction, scanning electron microscopy (EBSD-SEM) (Carlson, 1989, 1991; Spiess & Bell, 1996; Denison & Carlson,

1997; Denison *et al.*, 1997; Spiess *et al.*, 2001; Prior *et al.*, 2002; Hirsch *et al.*, 2003; Ketcham, 2005).

Several nucleation and growth models are proposed in the literature to account for the compositional zoning, crystal sizes and spatial distribution of garnet in metamorphic rocks derived from different sedimentary and igneous protoliths. Based on classical studies of garnet size and spatial distribution, Kretz (1969) and Carlson (1989, 1991) proposed that the rate-limiting step for garnet porphyroblast growth is the intergranular diffusion of the necessary chemical components. In such a model, the spatial distribution of garnet nuclei and the final size of porphyroblasts are controlled by competitive growth of nuclei that limits the availability of components, inhibiting further nucleation of nearby porphyroblasts. Other authors have emphasized the role of other factors, such as a potential microstructural control on the site of porphyroblast nucleation and growth due, among other factors, to partitioning of deformation (Spiess & Bell, 1996), and/or preferential nucleation and growth on reactant precursor phases (Spiess *et al.*, 2007).

Electron backscatter diffraction has proved to be an extremely useful tool to survey garnet microstructures in metamorphic rocks (Whitney *et al.*, 2008 and references therein). Polygonal textures, and low- and high-angle boundaries in metamorphic garnet can easily be detected in EBSD maps of crystallographic orientation. Although more attention has been paid to the influence of *P–T* conditions on the deformation mechanisms of garnet (Kleinschrodt & McGrew, 2000; Prior *et al.*, 2000, 2002; Kleinschrodt & Duyster, 2002; Mainprice *et al.*, 2004; Storey & Prior, 2005), several recent studies focused on garnet growth mechanisms using orientation distribution data (Spiess *et al.*, 2001, 2007; Hirsch *et al.*, 2003; Storey & Prior, 2005; Whitney *et al.*, 2008).

This paper presents a microstructural EBSD-SEM and TEM study of garnet growth in high-pressure mafic garnet granulites formed by dehydration melting of hornblende-gabbronorite protoliths in the Jijal complex (Kohistan palaeo-island arc complex, north Pakistan) (Jan, 1979; Jan & Howie, 1981; Yamamoto, 1993; Yamamoto & Yoshino, 1998; Yoshino *et al.*, 1998; Yoshino & Okudaira, 2004; Garrido *et al.*, 2006, 2007; Dhuime *et al.*, 2007). High-pressure garnet granulites developed after a low-pressure hornblende-gabbronorite protolith through a sharp reaction front at both outcrop and thin-section scales. This sharp transformation boundary provides a unique opportunity to study, at the thin-section scale, the role of precursor phases on the nucleation and growth of garnet, as well as to constrain the factors controlling the growth of garnet porphyroblasts and their habit variations. In concordance with recent studies (Spiess *et al.*, 2007), in the absence of deformation, the orientation of mafic precursor phases conditioned the nucleation site and led to the oriented growth of garnet due to topotaxial transformation reactions (i.e. reactions where a crystallographic relationship exists between reactant and product phases across interfaces) and to homoepitaxial growth (overgrowth of the same phase without lattice mismatch) of garnet. As a consequence, the orientation and texture of precursor phases fully determined the nucleation sites and the orientation of garnet during the formation of high-pressure, mafic garnet granulite after low-pressure mafic protoliths.

SAMPLE SELECTION AND METAMORPHIC CONDITIONS

A composite sample (KG-03) was selected from the Jijal complex (north Pakistan) that preserves the transition from precursor hornblende-gabbronorite to garnet granulite (Garrido *et al.*, 2006). The thin section shows a sharp, millimetre-scale transition (dotted line in Fig. 1) between the low-pressure precursor hornblende-gabbronorite and the garnet granulite product assemblage, which covers about 40% of the investigated thin section (Fig. 1a,b). A magmatic foliation in the hornblende-gabbronorite is defined by mafic-rich layering (dashed line *L in Fig. 1); the associated magmatic lineation is defined by the shape-preferred orientation (SPO) of mafic clusters composed of Opx + Cpx + Amp + oxides (Zeilinger, 2002). The shape of the reaction front is convoluted and oblique to the magmatic layering (RF in Fig. 1). The thin section was cut to ensure that precursor and reactant phases were both present in the same thin section, so the XY reference frame is arbitrarily set.

The intensity of the magmatic fabric is weak in the studied area. The foliation is on average 40° NW-dipping and the lineation plunges 35° NW (Zeilinger, 2002). The magmatic foliation is replaced locally by a higher intensity, regional tectonic fabric that is not observed in this sampling locality (Zeilinger, 2002).

Conventional thermobarometry, based upon selected exchange and net-transfer reactions involving garnet-clinopyroxene-plagioclase-quartz and Fe-Mg exchange thermometers and implemented with the GTB software (Spear & Kohn, 2001), yields equilibration pressures of 1.0–1.2 GPa and temperatures in the range of 810–825 °C for the formation of garnet granulite. If Fe^{3+} in clinopyroxene is taken into account, slightly lower equilibration pressures and temperatures are obtained ($1.0 < P < 1.1$ GPa; $735 < T < 750$ °C). These *P–T* estimates are in good agreement with previous studies (Yamamoto, 1993; Yoshino *et al.*, 1998; Yoshino & Okudaira, 2004) and with pseudosection thermodynamic calculations (PERPLE_X software; Connolly, 1990; Connolly & Petrini, 2002; and the updated version of the internally consistent thermodynamic database of Holland & Powell, 1998) of mineral composition isopleths for this sample (1.1–1.2 GPa; 825–875 °C) (J. A. Padrón-Navarta *et al.*, unpublished data).

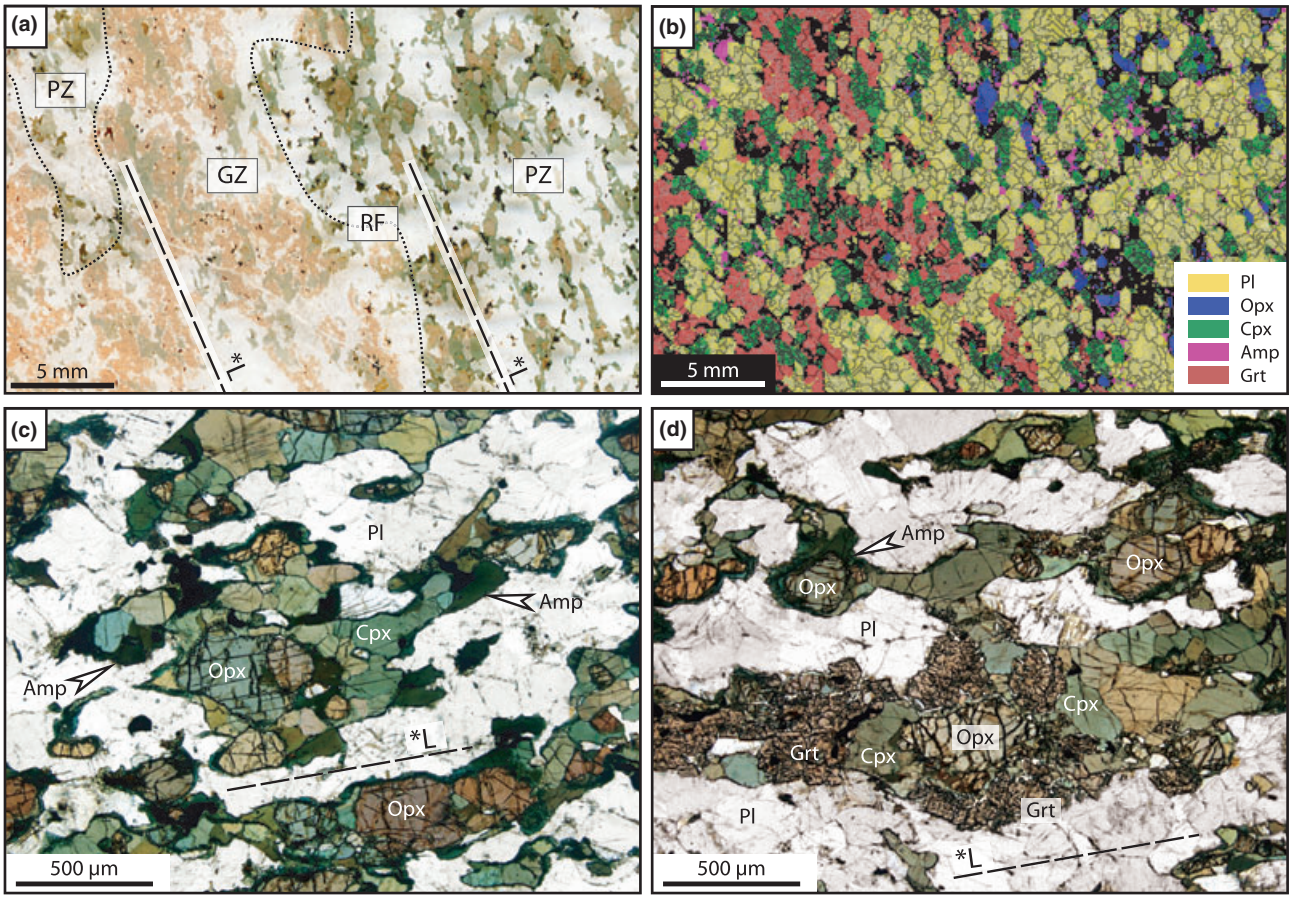

Fig. 1. (a) Scanned thin section of composite sample KG-03 showing the sharp and convolute reaction front (RF, dotted lined) between the zone with hornblende-gabbronorite (PZ, precursor protolith zone) and the high-pressure garnet granulite zone (GZ). Also shown is the trace of the foliation defined by the magmatic layering (*L) in the precursor hornblende-gabbronorite (PZ) that is cut by the PZ. Note that the trace of the foliation (*L) is still recognized in the garnet granulite zone (GZ). Compare with (b) for phase identification in the two zones. (b) Phase map of the same thin section shown in (a). The colour phase map was obtained by EBSD-SEM automated mapping and indexing in a 100 μm mesh, rectangular grid. (c) Micrograph of the PZ showing the aligned mafic clusters characteristics of the precursor, hornblende-gabbronorite. The cluster are composed of cores of orthopyroxene (Opx) surrounded by clinopyroxene (Cpx) and amphibole-oxides (plane-polarized light). (d) Micrograph showing the RF where garnet corona overgrows mafic clusters. The elongated shape of former mafic cluster can be still recognized. *L is shown in (a,b) as dashed line.

ANALYTICAL METHODS

Scanning electron microscopy

Scanning electron microscope (SEM) observations were performed by secondary and back-scattered electron imaging in carbon-coated polished thin sections using a Zeiss DMS instrument at the Centro de Instrumentación Científica (CIC) of the Universidad de Granada (Spain). The SEM was operated at an acceleration voltage of 20 kV. To carry out 3D SEM observations of garnet aggregates, the sample was crushed in an agate mortar and plagioclase-garnet aggregates concentrated by means of a Frantz magnetic separator. Aggregates were then leached several minutes with cold 5 N nitric acid to selectively remove plagioclase. Leached garnet aggregates were hand-picked under a binocular microscope, mounted on a sample holder and carbon-coated for SEM observation.

Electron backscatter diffraction-scanning electron microscopy

Mapping of the LPO of garnet, clinoamphibole (pargasite), orthopyroxene, clinopyroxene and plagioclase was performed by indexation of EBSD patterns. To improve the quality of Kikuchi diffraction patterns, standard diamond-polished (0.25 μm grain size) thin sections were further polished for 5 min with a chemical–mechanical procedure using colloidal silica suspension (Buehler™ Mastermet™). EBSD measurements were performed on a JEOL JSM 5600 SEM at Géosciences Montpellier (CNRS-Université de Montpellier 2, Montpellier, France) using a ~17 kV accelerating voltage and a working distance of 25 mm.

EBSD patterns were collected in the uncoated thin section, tilted at 20° to the vertically incoming electron beam and taped on the sample holder with conductive adhesive carbon tape. Automated EBSD mapping of the whole thin sections was acquired in a 100-μm mesh, rectangular grid. EBSD patterns were indexed automatically using CHANNEL 5 software package from HKL Technology. Lattice orientation by CHANNEL 5 software is achieved by automatic indexation of Kikuchi patterns using the Hough transform and six to nine detected band edges and their zones axis in the diffraction pattern. To index diffraction patterns of garnet, a pyrope end-member reflector file was used (Meagher, 1975). The other minerals were indexed using the standard Channel reflector file database. The EBSD data were processed and contoured as conventional CPO pole figures for selected crystallographic planes and directions using the software PFCH5 (Mainprice, 1990, 2007; Mainprice & Humbert, 1994).

Transmission electron microscopy

Selected areas of thin sections were detached from thin sections in copper grids, ion-milled and carbon coated for transmission electron microscopy (TEM) observation. Samples were examined using a Philips ^{TM} CM20 instrument at the CIC of the Universidad de Granada, operated at 200 kV and equipped with an energy-dispersive X-ray (EDX) model EDAX system for analytical electron microscopy applications. Reflections with d-values < 0.4 nm on selected-area electron diffraction patterns (SAED) were used to obtain crystal lattice images. STEM microanalyses were carried out using a 5-nm beam diameter and a scanning area of 1000 nm $\times$ 20 nm.

PETROGRAPHY

For descriptive purposes, the studied thin section can be subdivided into three zones: a precursor zone (PZ), the reaction front (RF) and the garnet granulite zone (GZ) (Fig. 1a). The PZ shows the reactant magmatic assemblage consisting of Pl + Cpx + Opx + Amp + Qtz + oxides (hornblende gabbronorite) (Fig. 1c). The GZ contains only the product assemblage that is composed of Pl + Cpx + Grt + Qtz + Rt (garnet granulite). Both areas are separated by a thin RF where product and reactant phases coexist.

Garnet first occurs at the RF as films grown ($\sim$ 200 μm thick) over precursor mafic clusters (aggregates of subhedral to anhedral orthopyroxene surrounded by clinopyroxene and amphibole) (Figs 1d & 2). Inclusions of precursor amphibole in garnet show their {110} cleavage planes subparallel to one of the rhombic dodecahedral {110} faces of garnet (Fig. 2a,b). Because of the preferential ion milling of amphibole relative to garnet, it has not been possible to inspect by TEM the garnet–amphibole interfaces to infer the relative crystallographic orientation between amphibole and garnet interface. However, the relative crystallographic orientation of garnet with secondary phyllosilicate after amphibole (altered to chlorite/smectite as confirmed by TEM and AEM observations) was successfully inferred, which allows retrieving the original crystallographic orientation between amphibole and garnet (Fig. 2a,c). The SAED pattern shows that phyllosilicate (001) planes are parallel to (112) garnet planes (trapezohedron faces) (Fig. 2d). The garnet habit and its interface shape with mafic minerals and plagioclase show gradual variations from the RF to the GZ. At the RF, garnet shows coronitic textures around mafic minerals showing sharp, planar interfaces with plagioclase (Fig. 3a). K-feldspar and quartz films are present in many of the plagioclase–garnet interfaces. Garnet coronitic aggregates around a given mafic cluster are composed of euhedral garnet aggregates with sub-parallel crystal faces (Fig. 3b). Three-dimensional, secondary electron SEM images of these garnet aggregates confirm that they are constituted by crystal aggregates of garnet with rhombic dodecahedral {110} habits (Fig. 3b).

Towards the mafic minerals, the garnet coronitic aggregates display a graphic texture consisting of garnet intergrowths with quartz, evolving inwards to quartz aggregates surrounding cores with relict hornblende and/or orthopyroxene, or secondary clinopyroxene and/or oxides (Fig. 3a). The skeletal garnet intergrowth shows hopper and skeletal morphologies with quartz inclusions (Fig. 3c,d), which, in places, are subparallel to garnet rhombic dodecahedral faces (Fig. 3d). The hopper and skeletal garnet morphologies are indicative of enhanced garnet growth at rhombic dodecahedral corners (Fig. 3c,d). This is confirmed by TEM imaging of the inner aggregates that shows how garnet skeletal and hopper morphologies with quartz develop at the nano-scale (Fig. 4), indicating that the rate of growth normal to the rhombic dodecahedral garnet faces was higher at the crystal corners than at the crystal faces (Fig. 4). In the GZ, the coronitic garnet intergrowths tend to be less common. In this zone, garnet aggregates are somehow transformed in large single crystals with few quartz inclusions and irregular shapes with embayments filled by coarse quartz aggregates.

LATTICE-PREFFERED ORIENTATION

The LPO of reactant and product mafic minerals (Opx, Amp, Cpx and Grt) in the composite sample KG-03 was investigated by means of EBSD-SEM (Fig. 1a). This technique allows the characterization of the crystallographic orientation of precursor and product minerals at the scale of the thin section, providing a statistically significant investigation of the LPO relationships among reactant and product assemblages at larger length-scales than those permitted by TEM observations (Prior *et al.*, 2002; Spiess *et al.*, 2007).

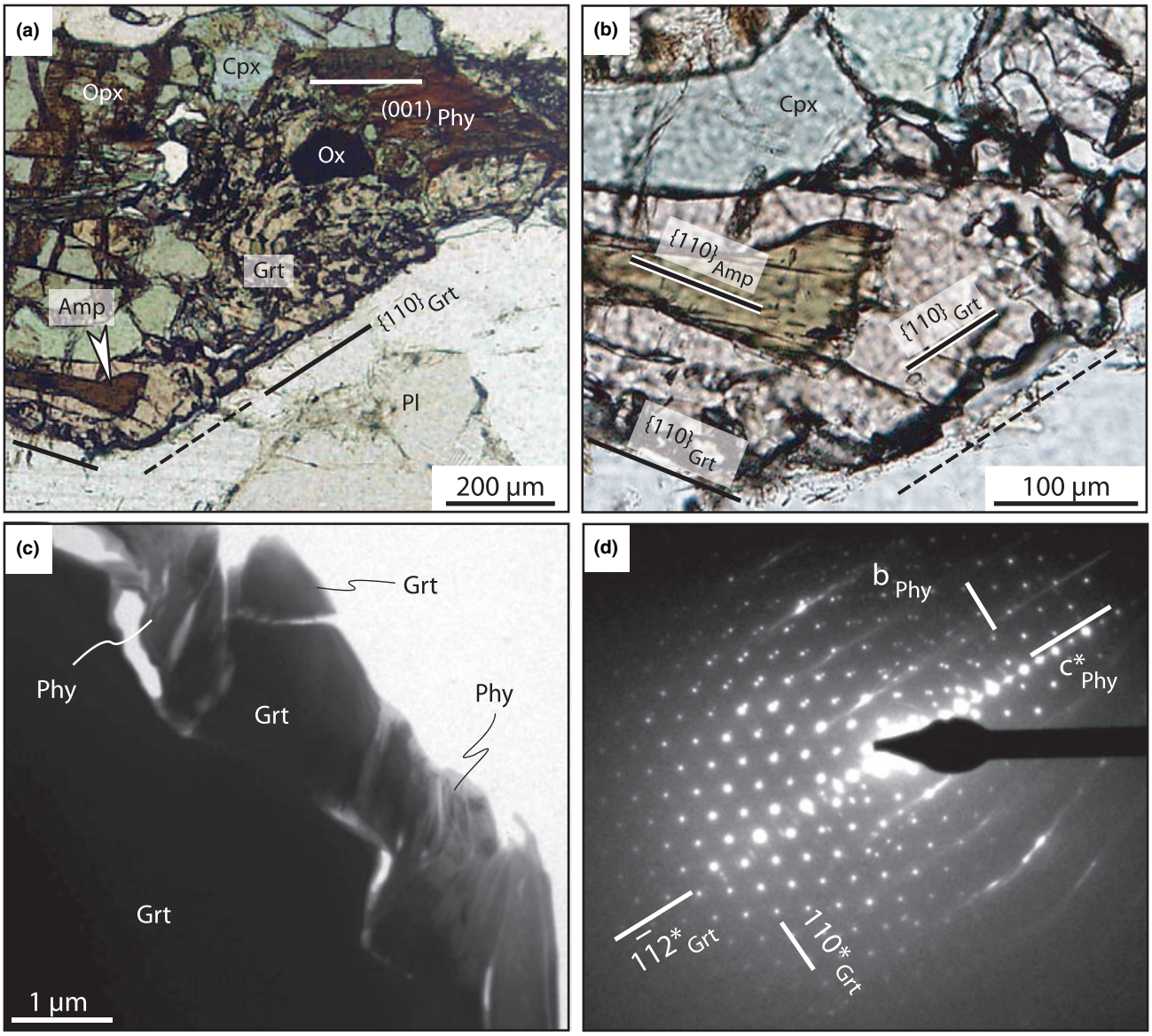

Fig. 2. (a) Micrograph of a partly transformed mafic cluster at the reaction front of sample KG-03. The mafic cluster is composed of a core of orthopyroxene (Opx) rimmed by clinopyroxene (Cpx), hemato-ilmenite (Ox) and amphibole (Amp) that is partly transformed to phyllosilicate (Phy). The cluster is overgrown by garnet (with quartz inclusions) showing a sharp interface (trace of rhombic dodecahedral faces) with plagioclase (Pl). Garnet preserves inclusions of precursor amphibole (parallel nicols); (b) Zoom of (a) showing the amphibole inclusion in garnet and the inferred orientation relationships between amphibole cleavage {110} and rhombic dodecahedral {110} faces of garnet; (c) TEM image of the garnet-phyllosilicate interfaces. Phyllosilicate spacing is consistent with a chlorite/smectite intergrown. (d) SAED of the garnet-phyllosilicate interface shown in (c). The SAED shows that phyllosilicate (001) planes are parallel to (112) garnet planes.

Figure 5 shows contoured pole figures of the LPO of mafic silicates in the composite sample KG-03. As the sample was cut to ensure that both precursor and reactant phases were present in the same thin section (Fig. 1a), the XY reference frame of pole figures does not correspond to the foliation and lineation plane. The magmatic foliation and lineation, which are defined by the alignment of mafic clusters and their SPO in the precursor hornblende gabbronorite (Fig. 1a), are depicted as a great circle (white continuous line) and a red star, respectively, in the pole figures (Fig. 5). The strength of the orientation of each crystallographic axis or sharpness of the pole figure is quantified by the *pfJ* index (Fig. 5). The *pfJ* index is related to the *J* index (Mainprice & Silver, 1993; Michibayashi & Mainprice, 2004) that is calculated using the orientation distribution function from the triplet of Euler angles (Bunge, 1982). However, the *pfJ* index for a given crystal direction cannot be compared among different minerals as it depends on

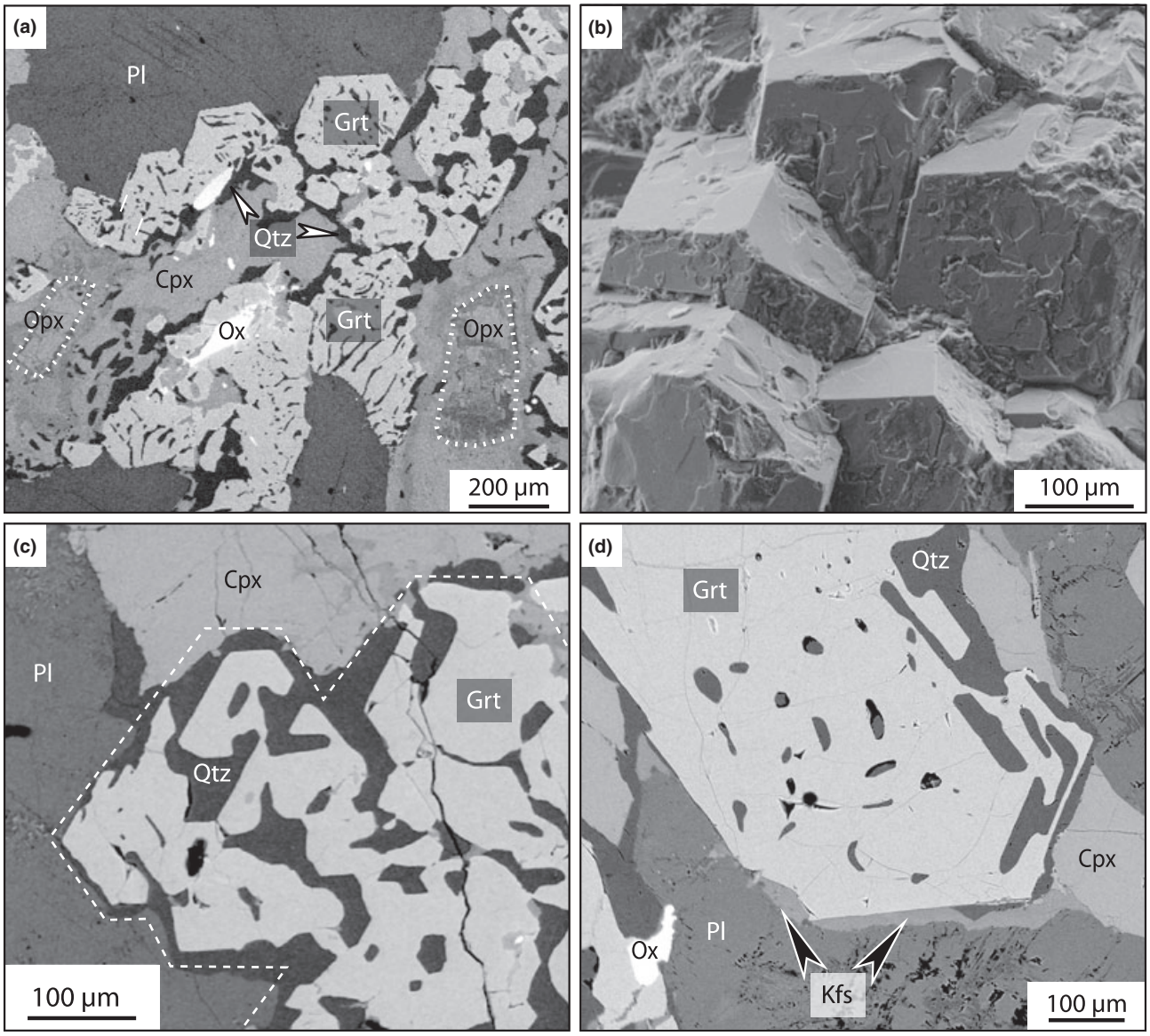

Fig. 3. (a) Garnet corona overgrowing previous orthopyroxene (Opx, dashed lines) – clinopyroxene (Cpx) mafic clusters. Quartz (black zones) is more abundant towards the contact with clinopyroxene. (b) SE-SEM 3D image of garnet coronitic structures around mafic clusters, showing that they are composed of parallel aggregates of rhombic dodecahedra. (c) Detail of the garnet-clinopyroxene contact showing hopper morphologies in the garnet crowded with quartz inclusions. Note that garnet is a single crystal (grain boundaries are shown by white dashed lines) and the re-entrants are filled by quartz. (d) K-feldspar (Kfs, arrowed) film in the garnet–plagioclase boundary grain where garnet shows euhedral faces. In contrast garnet and clinopyroxene are divided by skeletal quartz inclusions subparallel to incipient/starting rhombic dodecahedral garnet faces.

the crystal symmetry (Michibayashi & Mainprice, 2004).

Orthopyroxene and amphibole, the main mafic precursor phases of garnet, are only present in the gabbronorite zone and at the reaction front (PZ and RF, respectively, in Fig. 1a). Orthopyroxene, amphibole and, to a lesser extent, clinopyroxene, show a strong LPO that is intimately related to the magmatic foliation and lineation in the precursor hornblende-gabbronorite. Their [001] axes are largely contained in the foliation plane with a maximum subparallel to the lineation (Fig. 5a–c). Orthopyroxene displays the strongest LPO ($pfJ_{[100]}$ = 3.49 and $pfJ_{[001]}$ = 3.07; Fig. 5a) characterized by the alignment of [100] axes normal to the foliation and a girdle distribution of [001] axes in the foliation plane with a strong maximum subparallel to the lineation (Fig. 5a). Garnet aggregates also display a strong LPO (Fig. 5d). The lower *pfJ* index for ⟨111⟩ and ⟨110⟩ axes relative to the ⟨100⟩ axis in garnet pole figures is due to symmetry effects. Garnet LPOs show a maximum density distribution resembling that of a single-crystal of garnet

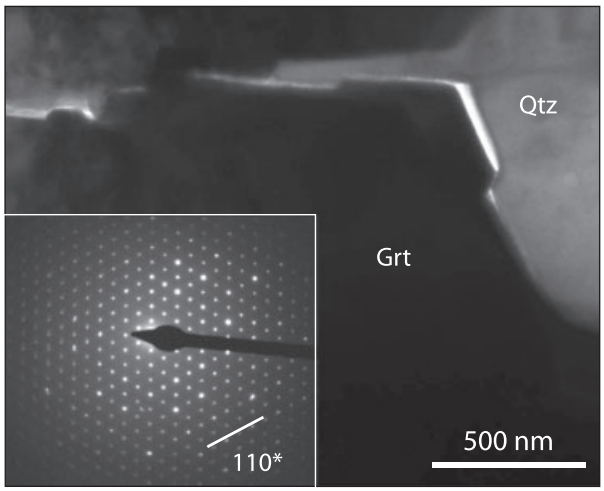

Fig. 4. TEM image of a garnet–quartz interface of graphitic intergrowth of garnet showing skeletal garnet morphologies demonstrating enhanced garnet growth at the crystal corners of rhombic dodecahedral garnet faces. Inset (lower left): SAED showing the garnet orientation.

with two of the four ⟨111⟩ axes within the magmatic foliation plane, one of them subparallel to the magmatic lineation (Fig. 5d).

The strength and the symmetry of the crystals' orientation distribution (i.e. random, point or girdle distribution) can be quantified by eigenvector analysis of the poles to (*hkl*) planes and [*uvw*] directions (Woodcock & Naylor, 1983; Vollmer, 1990). The eigenvalues of these orientations for KG-03 mafic minerals are given in Table 1 and the three eigenvectors (S_1, S_2 & S_3) for each mineral are plotted on the pole figures (Fig. 5). The strongest concentration is given by the eigenvector with the greatest eigenvalue and the pole to the best plane by the smallest eigenvalue for each crystallographic direction. The shape of the orientation distribution and its strength can be quantified by the ratios of eigenvalues and by the shape parameter, K [$K = \ln(S_1/S_2)/\ln(S_2/S_3)$] (Woodcock & Naylor, 1983). A cluster distribution of orientation data is characterized by $S_1 > S_2 \approx S_3$ and $K > 1.0$, with a $K = \infty$ for a uniaxial cluster distribution, whereas a girdle distribution is characterized by a $S_1 \approx S_2 > S_3$ and $K < 1.0$, with $K = 0$ for a perfect uniaxial girdle distribution. On the other hand, the randomness of the distributions may be expressed by the strength or critical parameter, C ($C = S_1/S_3$). The eigenvalues of a perfect uniform distribution are equal and hence $C = 1$, whereas a strong fabric has high C values.

Table 1 gives the computed K, C and eigenvalues of the poles to selected (*hkl*) planes and [*uvw*] directions for KG-03 mafic minerals. The three eigenvectors (S_1, S_2 & S_3) for each mineral are also plotted on their corresponding pole figure (Fig. 5). Eigenvector analysis is strictly valid for non-orthorhombic symmetries, but it used here, along with the *pfJ* index, to explore quantitatively the strength of the correlation and type of orientation distribution of crystallographic axes and planes of orthopyroxene, clinopyroxene, amphibole and garnet.

Orthopyroxene is characterized by a strong cluster distribution ($K = 1.84$, $C = 7.70$) of [100] axes and a strong girdle distribution of [001] axes ($K = 0.40$, $C = 11.43$) with a maximum concentration, marked by the S_1 eigenvector (347.6°/27.1°), that is subparallel to the magmatic lineation (Fig. 5a). For amphibole, the eigenvector of the poles to (100) is normal to the foliation plane (72.7°/9.7°) and, similarly to orthopyroxene, the poles to (001) and of the [001] axes show a girdle distribution around it on the foliation plane ($K = 0.79$, $C = 3.76$) with a maximum concentration (335.8°/35.91° and 338.1°/38.4°, respectively) subparallel to the lineation (Fig. 5b). The LPO of clinopyroxene is more scattered and, in contrast to what is observed for orthopyroxene and amphibole, clinopyroxene [010] axes are strongly clustered almost normal to the foliation (73.5°/13.0°; $K = 2.66$; cf. $K_{[010]}$ of other minerals in Table 1). Clinopyroxene poles to (001) and [001] axes have a girdle distribution in the foliation plane ($K = 0.65$ and 0.96, respectively) with a weak maximum close to the lineation (Fig. 5c).

Summing up, the EBSD study shows that both precursors and product minerals have a strong LPO that is intimately related to the magmatic lineation and foliation, which are defined by the SPO of mafic clusters. Precursor amphibole and orthopyroxene show poles to (001) and [001] axes clustered within the magmatic foliation, with a strong concentration subparallel to the lineation. A weaker, but similar crystallographic fabric is observed for clinopyroxene. On the other hand, garnet aggregates in the RF and the GF display a surprisingly strong orientation characterized by alignment of two of the ⟨111⟩ on the foliation plane, with one of them parallel to the magmatic lineation of the precursor hornblende gabbronorite zone. These orientation relationships suggest that the orientation of precursor, magmatic phases exerted a strong crystallographic control on the growth of garnet.

DISCUSSION

Origin of the LPO of precursor phases

An important finding of this study is the strong control that the LPOs of precursor, hornblende-gabbronorite minerals exerted on the oriented growth of garnet during high-pressure granulite metamorphism. Hence, the first requirement is to understand the origin of the observed LPO in hornblende gabbronorite precursor minerals and its close orientational relationships with magmatic layering and lineation.

Although crystal-plastic deformation by dislocation creep with dominant activation of the high-temperature

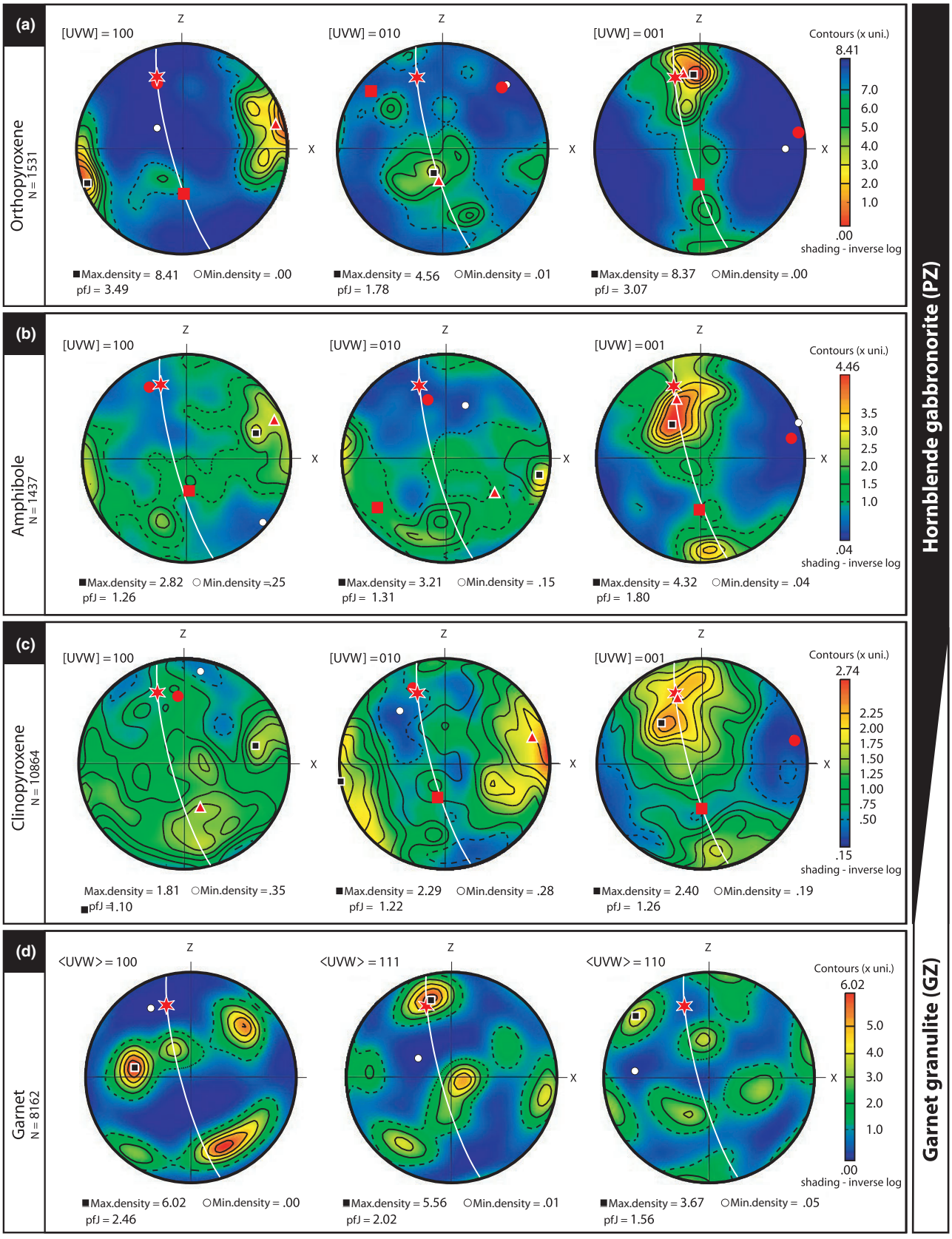

Table 1. Summary of EBSD data for sample KG-03 processed using software PFCH5 (Mainprice, 1990, 2007; Mainprice & Humbert, 1994).

Phase	n	Type	S_1	Dec	Inc	S_2	Dec	Inc	S_3	Dec	Inc	K	C
Opx	1531	*a*-axis	0.7161	75.16	8.57	0.1909	177.50	54.74	0.0930	339.30	33.90	1.84	7.70
		b-axis	0.4970	186.80	65.27	0.3180	308.90	13.76	0.1850	44.01	20.13	0.83	2.68
		c-axis	0.6310	347.60	27.06	0.3140	181.80	62.22	0.0550	80.59	5.84	0.40	11.43
Cpx	10864	*a*-axis	0.3811	158.78	54.50	0.3422	259.63	7.65	0.2767	354.92	34.42	0.51	1.38
		[100]	0.3932	179.98	49.10	0.3287	274.06	3.53	0.2781	7.10	40.68	1.07	1.41
		b-axis	0.4672	73.45	13.04	0.2902	190.30	62.85	0.2427	337.70	23.37	2.66	1.93
		c-axis	0.4690	339.91	34.04	0.3184	179.81	54.31	0.2126	76.38	9.47	0.96	2.21
		[001]	0.4754	340.19	30.55	0.3324	189.90	55.80	0.1923	78.58	13.88	0.65	2.47
Amp	1437	*a*-axis	0.4425	66.33	8.91	0.3148	175.39	64.37	0.2427	332.36	23.82	1.31	1.82
		[100]	0.4725	72.70	9.71	0.3024	176.38	54.13	0.2251	336.04	34.14	1.51	2.10
		b-axis	0.4021	124.96	42.54	0.3734	234.40	19.94	0.2245	342.64	40.78	0.15	1.79
		c-axis	0.5484	338.08	38.38	0.3058	181.46	49.21	0.1457	77.54	11.72	0.79	3.76
		[001]	0.5258	335.84	35.91	0.2951	176.45	52.27	0.1791	73.21	10.05	1.16	2.94
				Max. density									
Grt	8162	⟨111⟩		345.00	25.00								

S_1, S_2 and S_3 are the maximum, intermediate and minimum normalized eigenvalues respectively. n = number of patterns indexed.
Dec, declination; Inc, inclination.
Shape parameter, $K = \ln(S_1/S_2)/\ln(S_2/S_3)$ and strength parameter $C = S_1/S_2$ (Woodcock & Naylor, 1983).

(100)[001] system for orthopyroxene (Coe & Kirby, 1975; McLaren & Etheridge, 1976; Mercier, 1985; Dornbush *et al*., 1994) and (010)[001] system for clinopyroxene (Bascou *et al*., 2002; Terry & Heidelbach, 2006) may account for the observed LPO of pyroxene in the hornblende gabbronorite zone, at the petrographic and TEM scales there is no microstructural evidence for subsolidus crystal-plastic deformation (i.e. dynamic recrystallization, ribbon grains, undulose extinction, kink bands or subgrain boundaries) in precursor minerals.

Rigid-body rotation of elongated mafic minerals or clusters during magmatic flow at supersolidus conditions (Nicolas & Ildefonse, 1996; Lamoureux *et al*., 1999; Yoshinobu & Harper, 2004) is the most plausible mechanism, accounting for the LPO of Opx and its strong correlation with the SPO of mafic clusters in the hornblende gabbronorite. Textural observations show that crystallization of orthopyroxene occurred first, followed by clinopyroxene, amphibole and oxides, and that the two later phases formed at the waning stages of crystallization (Fig. 1a). The similarity between orthopyroxene and clinopyroxene LPO can be accounted for by either topotactic growth of magmatic clinopyroxene on earlier crystallized orthopyroxene or by rigid rotation of clinopyroxene crystals during magmatic flow. Amphibole and oxides tend to rim mafic clusters, replacing earlier clinopyroxene and orthopyroxene (Fig. 1c). These replacement textures are common in arc-derived hornblende-gabbronorite. They are formed due to peritectic reactions between amphibole and pyroxene on cooling in closed-system crystallization or *in situ* crystallization, or to late replacement by evolved melt/fluids (Arculus & Wills, 1980; Conrad & Kay, 1984; Fichaut *et al*., 1989; Costa *et al*., 2002). As crystallization of amphibole occurs at small melt fractions when magmatic flow is unlikely (Nicolas & Ildefonse, 1996), the similarity between amphibole and pyroxene LPO is better explained by the well-known topotactic relation between amphibole and pyroxene during near-solidus peritectic reactions (Thompson, 1978).

Crystallographic relationships between garnet and precursor phases

This textural study indicates that the LPO of precursor magmatic phases controlled the oriented growth of garnet during high-pressure garnet granulite metamorphism. The [001] axes of precursor pyroxene and amphibole are contained within the magmatic layering plane and are subparallel to the magmatic lineation (Fig. 5c). The garnet-in reaction was a reconstructive topotatic reaction in the sense of Figlarz *et al*. (1990), because garnet took advantage of the crystal lattices of precursor phases as substrates for its oriented growth.

Petrographic and textural observations indicate that garnet first nucleated on precursor amphibole surrounding mafic clusters (Figs 1b,d & 2). TEM observations (Fig. 2) show that retrograde phyllosilicates (Phy) in contact with garnet display the following crystallographic relationships (Fig. 2b,d):

$$[110]_{\mathrm{Grt}}//b_{\mathrm{Phy}},\quad [1\bar{1}2]_{\mathrm{Grt}}//c^{*}_{\mathrm{Phy}},\quad [\bar{1}11]_{\mathrm{Grt}}//a_{\mathrm{Phy}} \quad (1)$$

Fig. 5. Pole figures showing the LPO of orthopyroxene (a), amphibole (b), clinopyroxene (c), and garnet (d) in the composite sample KG-03. Pole figures are represented on lower hemisphere equal area projections. Foliation is represented by a continuous white line (pole to foliation plane, 75°/10°) and lineation of elongated mafic cluster by a red star. Filled contour in multiples of a uniform distribution (m.u.d.). N = number of patterns indexed used for plotting. Only clinopyroxene occurs in hornblende gabbronorite and garnet granulite zone. Amphibole and orthopyroxene are absent in the garnet granulite assemblages zone of sample KG-03. Maximum and minimum density values and the pole figure *J* index (*pf.J*) are also indicated. The three eigenvectors S_1, S_2, S_3 are plotted as red triangles, squares and dots respectively (for eigenvalues and their orientation, see Table 1).

where c^*_{Phy} denotes the direction normal to the $(001)_{Phy}$ planes (see Putnis, 1992 for the crystallographic notation used here; note that for clinopyroxene and amphibole c^*- and c-axes are not coincident). Phyllosilicate results from the well-known topotactic reaction after amphibole characterized by parallelism between [010] axes of amphibole and phyllosilicate, as well as parallelism between [001] axis of amphibole and [100] axes of phyllosilicates (Veblen, 1991, 1992):

$$b_{Amp}//b_{Phy}, \quad a^*_{Amp}//c^*_{Phy}, \quad c_{Amp}//a_{Phy} \qquad (2)$$

This topotactic reaction, along with the crystallographic relations observed between garnet and phyllosilicate (Eq. 1), suggests a topotactic replacement of garnet by amphibole characterized by:

$$[110]_{Grt}//b_{Amp}, \quad [1\bar{1}2]_{Grt}//a^*_{Amp}, \quad [\bar{1}11]_{Grt}//c_{Amp} \qquad (3)$$

This topotactic replacement is consistent with the petrographic observation showing that {110} garnet faces are parallel to the {110} amphibole cleavage (Fig. 2a,b). As the [001] axis of amphibole is subparallel to the magmatic lineation (Fig. 5b), the garnet topotactic reaction after amphibole (Eq. 3) caused garnet growth with two of its four ⟨111⟩ directions within the magmatic foliation, one of them subparallel to the magmatic lineation (Fig. 5d). This strong orientational relationship between reactant (amphibole, pyroxene and orthopyroxene) and product phases (garnet) implies that nucleation and growth of garnet were conditioned by the orientation of its precursor phases.

Figure 6 shows a cartoon of the lattice projections of garnet, amphibole, pyroxene and phyllosilicate, showing the above-inferred orientational relationships. These structural relationships minimize the mismatch between garnet and amphibole crystal lattices. Using published lattice parameters of amphibole and garnet, the lattice misfit at ambient temperature is ~9.5% along $[110]_{Grt}//b_{Amp}$ and 1% along $[112]_{Grt}//a_{Amp}$ (Fig. 3). A higher mismatch of ~20% is estimated along $[\bar{1}11]_{Grt}//c_{Amp}$.

The good orientational relationships of precursor amphibole and pyroxene in mafic clusters, which are in accordance with the well-known topotactic relationships in biopyroboles (Thompson, 1978), allow us to infer the overall crystallographic relationship between precursor, reactant phases (Opx, Cpx and Amp) and garnet as:

$$\langle 111\rangle_{Grt}//[001]_{Opx,Cpx,Amp} \qquad (4)$$

Although all the relative orientational relationships implied by this topotactic law have not been confirmed by TEM observations, this crystallographic relationship between mafic precursors and garnet accounts for the LPOs of garnet and its inheritance of the precursor magmatic fabric. Once amphibole was consumed in the reaction, the strong orientational relationship between mafic-phase reactants allowed the growth of garnet with the same orientation over a pyroxene substrate, eventually sintering into single-crystal garnet.

Finally, it is worth noting that, within the framework of the ionic model of crystal lattice, oriented growth of product phases on precursor minerals during topotactic reaction is customarily accounted for by the parallelism of their interfaces to planes with the highest density of framework oxygen closed-packing (Spry, 1969; Worden *et al.*, 1987). In the present case, the garnet and amphibole interfaces of the topotactic

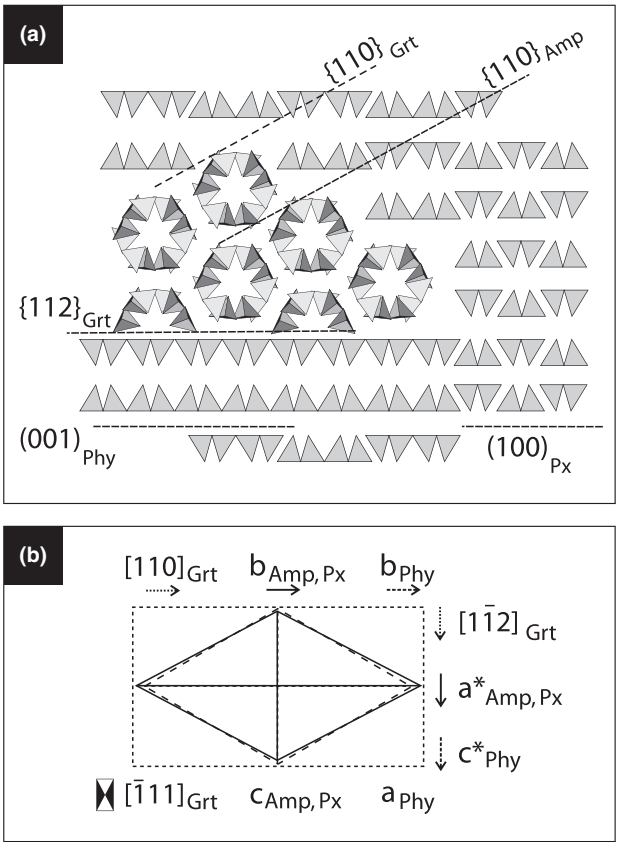

Fig. 6. (a) Projections of the polyhedral representation of the crystal lattice of garnet (Grt), amphibole (Amp), pyroxene (Px) and phyllosilicate (Phy) showing the orientational and dimensional relationships between the crystal lattices of these minerals inferred by TEM and EBSD orientation data and best explaining the topotactic reactions of garnet on amphibole substrates. The garnet lattice is projected down the ternary axis, that of amphibole down the [001] axis, and that of phyllosilicate down the *a*-axis. Only tetrahedra are shown for simplicity. The traces of mineral interfaces have also been drawn (cf. Fig. 2). Match among amphibole and garnet lattices (the solid, dashed and dotted lines correspond to amphibole, garnet and phyllosilicate lattices, respectively). Note that the topotaxial relationship between garnet and amphibole is $(110)_{Grt}//(110)_{Amp}$ and $[\bar{1}11]_{Grt}//[001]_{Amp}$ when is expressed as common plane and parallel direction respectively.

reaction of garnet after amphibole ($\{110\}_{Grt}//\{110\}_{Amp}$; Fig. 6) are inconsistent with this model. Garnet–amphibole interfaces (dotted line in Fig. 6; see also Fig. 2) are parallel to the periodic bond chains (PBC) (Hartman & Perdok, 1955), which are crystallographic directions with strong (i.e. more covalent) chemical bonds. Consequently, the attachment of amphibole-garnet tetrahedra across these interfaces corresponds to weak bonds involving cations other than Si.

Overstepping of garnet-forming reactions

From phase diagram constraints and *P–T* estimates, the precursor, hornblende gabbronorite assemblage remained metastable until the prograde amphibole breakdown reaction occurred. The sharp discontinuous modal and compositional variations observed at the reaction front attest to the role of kinetic inhibition of earlier prograde, solid-state reactions predicted by equilibrium-phase diagrams. In particular, the non-preservation of the predicted intermediate stages of replacement of orthopyroxene by garnet in the presence of stable amphibole is remarkable, considering the large *P–T* field ($P > 2$ kbar, Fig. 7) along the prograde path wherein this assemblage is stable. As the nucleation step is the main limiting step for the departure from equilibrium of metamorphic reactions (Rubie, 1998; Waters & Lovegrove, 2002), the metastability of the hornblende-gabbronorite assemblage indicates that garnet nucleation after orthopyroxene never overcame the kinetic barriers until the dehydration-melting breakdown reaction of amphibole occurred. The calculated phase diagrams indicate that melt released (~2–4%) by amphibole breakdown drove the system towards equilibrium by plagioclase dissolution, leading to the rapid exhaustion of metastable orthopyroxene. The most plausible explanation for reaction inhibition is the sluggish plagioclase dissolution under fluid-absent conditions, as is observed in experimental dehydration melting of a hornblende-plagioclase mixture of amphibolitic composition at 1000 °C and at 8 and 12 kbar (Johannes & Koepke, 2001).

Classical nucleation theory predicts that the nucleation probability is virtually zero until a threshold overstep of the reaction free energy is overcome (Ridley & Thompson, 1986; Lasaga, 1998; Rubie, 1998). The value of the critical overstep for nucleation is poorly constrained and there are important discrepancies between experimentally and naturally derived quantities. The relative amount of the reaction overstep can however be examined in terms of the amount of free energy relative to the target equilibrium reaction as a function of pressure and temperature ($\Delta G_{P,T}$), also known as the reaction affinity (A) (Ashworth & Sheplev, 1997; Ashworth *et al.*, 1998; Waters & Lovegrove, 2002). The affinity for a reaction ($-\Delta G_{P,T}$) involving a Θ total number of phases at

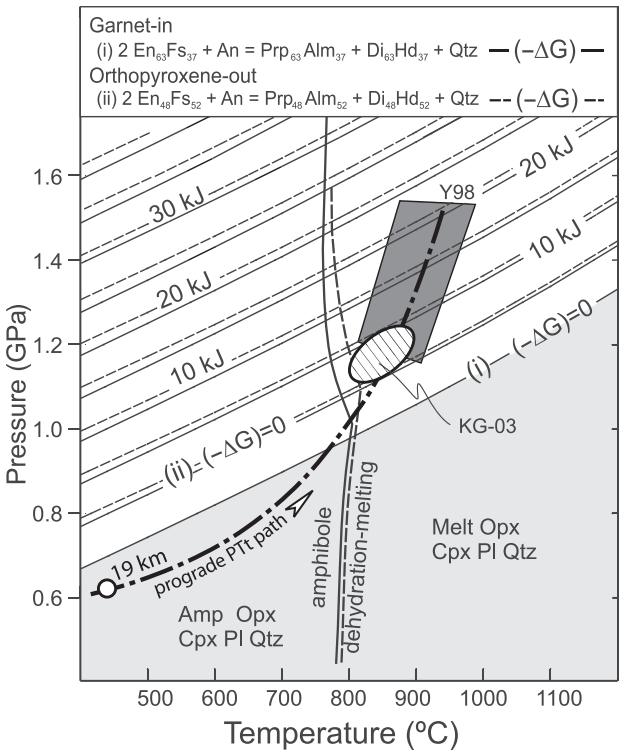

Fig. 7. Contours of the reaction overstep for garnet-in and orthopyroxene-out overall reaction (Eqs 6 and 7 respectively) in the CFMAS system in kJ per mol. of garnet produced. Computations were carried out using FRENDLY, a FORTRAN program included in the thermodynamic software package PERPLE_X (vs. 2007) (Connolly, 1990) using the internally consistent thermodynamic dataset of Holland & Powell (1998). Also, shown are the *P–T* conditions estimates for garnet granulite for the sample KG-03 (hatched) and those derived by Yoshino *et al.* (1998) and Yoshino & Okudaira (2004) (Y98). The grey field at low pressure shows the equilibrium assemblage without garnet in the hornblende gabbronorite assemblage. Amphibole dehydration-melting curve (solid line) and amphibole-out curve (dashed line) for KG-03 are those derived by (J. A. Padrón-Navarta *et al.*, unpublished data). *P–T–t* path inferred by thermal modelling and proposed for the evolution of the Kohistan lower crust for the case of intrusions intruded at initial depth of 19 km (white dot) in the double-plate model of Yoshino & Okudaira (2004).

constant *P–T* is the difference of molar free energy (G_k) among k-phases reactants and products balanced by their stoichiometry coefficients (υ_k) (Prigogine & Defay, 1954; Ashworth & Sheplev, 1997; Ashworth *et al.*, 1998):

$$(-\Delta G_{P,T}) = \sum_{k=1}^{\Phi} \upsilon_k G_k \qquad (5)$$

The first nucleation of garnet after orthopyroxene (Grt-in reaction) and the orthopyroxene exhaustion (Opx-out reaction) reactions in the simplified CFMAS system are (end-member abbreviation after Kretz, 1983):

$$2En_{48}Fs_{52} + An = Prp_{48}Alm_{52} + Di_{48}Hd_{52} + Qtz \qquad (6)$$

$$2En_{63}Fs_{37}+An = Prp_{63}Alm_{37}+Di_{63}Hd_{37}+Qtz \quad (7)$$

In these reactions, the compositions of garnet and orthopyroxene in the CFMAS system are obtained from pseudosection phase diagrams. Figure 7 shows the contours of the affinity in the *P–T* space calculated from thermochemical data for the foregoing reactions. The *P–T* field for the equilibration of Jijal garnet granulites establishes reaction affinities of ~5–10 kJ mol.$^{-1}$ for the Grt-in reaction (Eq. 6), and 0–5 kJ mol.$^{-1}$ for the Opx-out reaction (Eq. 7). These overstepping quantities are similar to those estimated for the formation of garnet coronas in mafic granulites (6.9 ± 1.8 kJ mol.$^{-1}$, Ashworth *et al.*, 1998), and those estimated for other metamorphic reactions (e.g. 5.0 kJ mol.$^{-1}$, Waters & Lovegrove, 2002; 5.6 ± 2.4 kJ mol.$^{-1}$; Baxter & DePaolo, 2002) and experimental studies (1.2–8.0 kJ mol.$^{-1}$; Ridley & Thompson, 1986; Ague, 2003 and references therein). Based on Monte Carlo simulation of natural garnet growth morphologies, Wilbur & Ague (2006) estimated an overstep of at least ~2 kJ mol.$^{-1}$ for garnet produced by muscovite and chlorite dehydration during Barrovian metamorphism. Thus, it can be concluded that for the Jijal Complex the garnet-forming reaction after orthopyroxene had a high affinity at the peak *P–T* equilibration conditions of the granulite assemblage. The very sharp dependence of the nucleation and growth rate on the reaction affinity entails very high nucleation and growth rates of garnet after metastable orthopyroxene.

Garnet nucleation and growth mechanisms

The spatial textural variation of garnet observed can be used to infer the temporal sequence of garnet nucleation and growth, as well as the different garnet growth mechanisms that operated during the transformation of hornblende-gabbronorite to garnet granulite. Textural observations indicate that the onset of garnet nucleation and growth occurred along plagioclase–amphibole interfaces. This is evidenced by rough interfaces composed of garnet films coating amphibole and by relatively flat interfaces with plagioclase (Figs 1d & 2a,b). This texture suggests that the first stage of the amphibole-breakdown reaction produced a fluid/melt film between amphibole and plagioclase, where garnet nucleated preferentially on amphibole interfaces.

The topotaxial orientational relationships inferred between garnet and amphibole suggest that oriented nucleation of garnet on the reactant amphibole substrate may have played a key role in overcoming the critical overstep for the amphibole-breakdown reaction. A topotaxial reaction equally accounts for heterogeneous nucleation of garnet on mafic clusters, which determined the spatial distribution of garnet porphyroblast in the GZ, and the inheritance of the hornblende-gabbronorite fabric. Topotaxial reactions in material science and mineralogy are commonly ascribed to solid-state transformation and reactions (Putnis, 1992). The onset of garnet growth most likely was a fluid/melt-present, interface-coupled dissolution–precipitation reaction, where garnet nucleation took place at the surface of amphibole. Variations of trace element contents and ratios in Jijal composite samples are more consistent with partial melting and segregation of low fractions of granitic melts (Garrido *et al.*, 2006). Oriented growth of the product phase because of dissolution–precipitation reactions can take place if there is a topotaxial crystallographic relationship between product and reactant phases (Putnis & Putnis, 2007). This onset stage of garnet nucleation and growth was characterized by stable planar surfaces and might correspond to a first stage of a two-dimensional nucleation growth mechanism (Sunagawa, 1987).

The second stage of growth is observed along the reaction front. It is characterized by development of garnet hopper crystal morphologies with numerous quartz inclusions (Fig. 3c). At the reaction front, hopper garnet morphologies are well developed where amphibole is exhausted, where metastable orthopyroxene is reacting, or where both precursor phases for garnet are absent. For a given mafic cluster, garnet hopper morphologies commonly develop inwards of the mafic clusters core, a textural location where orthopyroxene commonly occurs at the metastable hornblende-gabbronorite zone (Fig. 1). This observation suggests that garnet hopper morphologies are somehow related to the breakdown reactions of metastable orthopyroxene after the garnet nucleation and growth stage. The development of mono-crystalline garnet after a single mafic cluster (Fig. 3), the remarkable epitatic orientation of rhombic dodecahedral garnet of hopper interfaces (Fig. 3b), and the lack of independent nuclei of garnet within clusters point out that, for a given cluster, further growth of garnet nucleated in the first stage took place by a homoepitaxial growth mechanism (Quon & Potvin, 1972; Robertson, 1978; Markov & Stoyanov, 1987; Markov, 1995; Hibiya & Görnert, 2007; Spiess *et al.*, 2007) after exhaustion of amphibole.

Hopper garnet morphologies are known in magmatic crystallization under high undercooling (Kirkpatrick, 1981; Faure *et al.*, 2003) and in prograde regional metamorphism (Jamtveit & Andersen, 1992; Wilbur & Ague, 2006). Hopper crystal morphologies are produced by very fast rates of growth ('disequilibrium growth'; Kuroda *et al.*, 1987). The growth rate increases with variations of the somehow related magnitudes: the reaction affinity, heating rate (Ridley, 1985), supersaturation (Kuroda *et al.*, 1987) and the absolute temperature (Walther & Wood, 1984). It is unlikely that variations in absolute temperature or heating rate at the centimetre-scale may account for the observed disequilibrium growth of garnet inwards the core of mafic cluster. The development of garnet

hopper textures is most likely related to supersaturation triggered by the high affinity of the disequilibrium breakdown reaction of metastable orthopyroxene in mafic clusters (Eqs 6 & 7).

A first requirement is to understand why the kinetic barriers for the orthopyroxene-consuming reaction were overcome just at the reaction front. The textural sequence observed at the reaction front and the sharp front between metastable precursor assemblages at the thin-section scale point to the release of a fluid/melt phase by amphibole breakdown (Fig. 7) in the reaction front as the key factor expediting the breakdown of metastable orthopyroxene. The amphibole-breakdown reaction not only helped to surmount the critical step for the early nucleation of the garnet-forming reaction after orthopyroxene, but also released a fluid/melt phase. The main rate-limiting factor in solid-state garnet-forming reactions is the intergranular diffusion of the slowest diffusing major element participating in the reaction, which is Al in most garnet-forming metamorphic reactions (Ashworth & Sheplev, 1997; Ashworth *et al.*, 1998). The presence of an intergranular fluid phase increases the intergranular diffusion coefficient for Al by several orders of magnitude (Carlson *et al.*, 1995; Carlson, 2002). The enhanced intergranular diffusion of Al in a fluid/melt phase most likely overcome the kinetic barrier that had promoted the orthopyroxene metastability so far. The high affinity of the garnet-in reaction after orthopyroxene (Fig. 7) enhanced the dissolution rate of metastable orthopyroxene, generating a supersaturated solution at the interface between earlier nucleated garnet and orthopyroxene.

The mechanism of interfacial growth in fluid/melt epitaxy depends on various factors controlling the growth rate of the precipitating phase such as supersaturation, misfit (lattice mismatch) and strain (smooth or rough interface) with the substrate phase, and the presence of surfactants, among others (Sunagawa, 1987; Markov, 1995; Hibiya & Görnert, 2007). In a reaction mediated by a fluid/melt phase, the interfacial growth rate of the reaction product is directly proportional to the diffusion coefficient of the slowest diffusion element in the reaction and the supersaturation, and inversely proportional to the thickness of the diffusion boundary layer. A departure from the 2D growth mechanism of the interface with increasing supersaturation and growth rate is observed successively from step bunching, formation of inclusions, edge nucleation and surface dendrites, and hopper growth and bulk dendrites in the transition from stable growth to growth instability (Sunagawa, 1987; Markov, 1995; Hibiya & Görnert, 2007).

The 3D epitaxial growth implied by the hopper garnet interfaces was most likely caused by supersaturation. Once the kinetic barrier for the metastable garnet-in reaction after orthopyroxene was overcome, the high reaction rates – driven by the high affinity of the reaction – produced supersaturation of garnet components at the garnet–orthopyroxene interfaces. Supersaturation in garnet components sparked the growth rate (Kuroda *et al.*, 1987) of the garnet interface towards the core of mafic cluster by a homoepitaxial 3D growth mechanism resulting in the observed garnet single crystals with hopper morphologies at the reaction front. Supersaturation also accounts for enhanced growth rate of garnet crystal corners relative to crystal edges (Donaldson, 1976; Kirkpatrick, 1981; Kuroda *et al.*, 1987; Faure *et al.*, 2003) observed at the TEM nanoscale (Fig. 4). Fast garnet growth facilitated the formation of inclusions of quartz generated during orthopyroxene-breakdown reaction (Eqs 6 & 7). The development of faceted garnet commonly observed at the plagioclase–garnet interfaces is characteristic of 2D growth mechanisms, which are favoured by slow growth rates and reduced supersaturation (Kuroda *et al.*, 1987; Hibiya & Görnert, 2007).

The third stage of garnet growth was related to the final development of garnet porphyroblasts free of quartz inclusions observed in the GZ. The similar orientation between hopper garnet in the RF and large garnet porphyroblasts in the GZ, along with the close spatial relationship of porphyroblasts with mafic clusters, demonstrates that polyhedral garnet porphyroblasts derived from hopper garnet observed at the RF. The most likely mechanism whereby monocrystalline polyhedral garnet porphyroblasts may form after hopper garnet is by solution precipitation of quartz inclusions and coalescence of garnet hopper interfaces driven by a reduction of interfacial energy. Coalescence was favoured by the completion of garnet-producing net transfer reactions that reduced supersaturation and growth rate and by the high temperature at the granulite peak conditions (825–875 °C, Padrón-Navarta *et al.*, 2008). Both factors, enhanced by a fluid-phase, promoted annealing and coalescence, forming faceted garnet porphyroblasts, which represent the final equilibrium texture in the GZ.

Coalescence and clustering of initial randomly oriented nuclei to a preferred bulk orientation because of misorientation-driven rotation (Spiess *et al.*, 2001) has been proposed as a mechanism to produce garnet porphyroblasts with a strong CPO (Spiess *et al.*, 2001). However, polycrystalline garnet aggregates with high-angle boundaries (Whitney *et al.*, 2008) and garnet single crystals with identical orientation (Hirsch *et al.*, 2003) observed using orientation contrast imaging partially contradict this interpretation. The rotation mechanism predicted in the hypothesis of Spiess *et al.* (2001) is a function of temperature and it is expected to operate effectively under high-temperature conditions at granulite facies relevant to this study (>750 °C). However, detailed EBSD orientation maps of garnet of the Jijal Complex do not reveal any microstructural feature implying that the misorientation of initial nuclei at plagioclase–amphibole boundaries was small or alternatively that high-angle boundaries were suppressed by misorientation-driven rotation at the initial stages of growth. The lack of structural complexity

observed in garnet coronas or in garnet porphyroblasts is indeed better explained by topotactic nucleation of garnet at mafic cluster rims.

SUMMARY AND CONCLUSIONS

Mafic garnet granulites of the Jijal complex (Kohistan complex, north Pakistan) preserve a unique natural example of porphyroblast garnet nucleation and growth during high-pressure amphibole dehydration melting of hbl-gabbronorite, where the LPO fabric of precursor mafic minerals led to oriented growth of garnet. Garnet shows a strong LPO with two ⟨111⟩ axes on the foliation plane that can be accounted by the generalized topotaxial crystallographic relationships $\langle 111\rangle_{Grt}//[001]_{Opx,Cpx,Amp}$.

The following sequence of garnet formation after the precursor mafic minerals can be inferred:

1 A first stage of garnet nucleation on amphibole at the amphibole–plagioclase interface during the amphibole-breakdown reaction that led to a fast kinetic for garnet nucleation and growth favoured by the release of a fluid/melt phase. At this stage, the existence of a 3D fit between amphibole and garnet crystal lattices (topotaxy) allowed interface-controlled growth of garnet.

2 A second stage of skeletal garnet growth towards the inner part of single mafic clusters where garnet developed 'hopper' morphologies enclosing quartz inclusions. These garnet morphologies are accounted for by fast, 3D homoepitaxial garnet growth because of the high affinity of the garnet-producing reaction after metastable orthopyroxene that led to local supersaturation. The breakdown of metastable orthopyroxene was triggered by an increase of the intergranular diffusion of Al due to the presence of a fluid-melt phase.

3 A final stage of Ostwald ripening or crystal sintering resulted in the formation of large inclusion-free garnet porphyroblasts commonly observed in garnet granulites farther away from the reaction front.

ACKNOWLEDGEMENTS

The authors highly appreciate the reviews of J.J. Ague, D. Whitney and one anonymous reviewer which helped to improve the final version of the manuscript. This work was supported by the Spanish 'Ministerio de Ciencia e Innovación (MICINN)' through research grants CGL2006-04440, CGL2007-61205/BTE, and ACI2006-A9-0580, and by the 'Junta de Andalucía' research groups RNM-145 and RNM-131. JAPN is supported by fellowship AP2005-060 from the 'Programa de Formación del Profesorado Universitario' and CJG by a RyC fellowship, both granted by the Spanish MICINN.

REFERENCES

Ague, J. J., 2003. Fluid flow in the deep crust. *Treatise on Geochemistry*, **3,** 195–228.

Arculus, R. J. & Wills, K. J. A., 1980. The petrology of plutonic blocks and inclusions from the Lesser Antilles Island Arc. *Journal of Petrology*, **21,** 743–799.

Ashworth, J. R. & Sheplev, V. S., 1997. Diffusion modelling of metamorphic layered coronas with stability criterion and consideration of affinity. *Geochimica et Cosmochimica Acta*, **61,** 3671–3689.

Ashworth, J. R., Sheplev, V. S., Bryxina, N. A., Kolobov, V. Y. & Reverdatto, V. V., 1998. Diffusion-controlled corona reaction and overstepping of equilibrium in a garnet granulite, Yenisey Ridge, Siberia. *Journal of Metamorphic Geology*, **16,** 231–246.

Bascou, J., Tommasi, A. & Mainprice, D., 2002. Plastic deformation and development of clinopyroxene lattice preferred orientations in eclogites. *Journal of Structural Geology*, **24,** 1357–1368.

Baxter, E. F. & DePaolo, D., 2002. Field measurement of high temperature bulk reaction rates II: Interpretation of results from a field site near Simplon Pass, Switzerland. *American Journal of Science*, **302,** 465–516.

Bunge, H. J., 1982. *Texture Analysis in Materials Sciences*. Buttleworth, London.

Carlson, W. D., 1989. The significance of intergranular diffusion to the mechanisms and kinetics of porphyroblast crystallization. *Contributions to Mineralogy and Petrology*, **103,** 1–24.

Carlson, W. D., 1991. Competitive diffusion-controlled growth of porphyroblasts. *Mineralogical Magazine*, **55,** 317–330.

Carlson, W. D., 2002. Scales of disequilibrium and rates of equilibration during metamorphism. *American Mineralogist*, **87,** 185–204.

Carlson, W. D., Denison, C. & Ketcham, R. A., 1995. Controls on the nucleation and growth of porphyroblasts: kinetics from natural textures and numerical models. *Geological Journal*, **30,** 207–225.

Coe, R. S. & Kirby, S. H., 1975. Orthoenstatite to clinoenstatite transformation by shearing and reversion by annealing – mechanism and potential applications. *Contributions to Mineralogy and Petrology*, **52,** 29–55.

Connolly, J. A. D., 1990. Multivariable phase-diagrams: an algorithm based on generalized thermodynamics. *American Journal of Science*, **290,** 666–718.

Connolly, J. A. D. & Petrini, K., 2002. An automated strategy for calculation of phase diagram sections and retrieval of rock properties as a function of physical conditions. *Journal of Metamorphic Geology*, **20,** 697–708.

Conrad, W. K. & Kay, R. W., 1984. Ultramafic and mafic inclusions from Adak-island: crystallization history, and implications for the nature of primary magmas and crustal evolution in the Aleutian arc. *Journal of Petrology*, **25,** 88–125.

Costa, F., Dungan, M. A. & Singer, B. S., 2002. Hornblende- and phlogopite-bearing gabbroic xenoliths from Volcan San Pedro (36 degrees S), Chilean Andes: evidence for melt and fluid migration and reactions in subduction-related plutons. *Journal of Petrology*, **43,** 219–241.

Denison, C. & Carlson, W. D., 1997. Three-dimensional quantitative textural analysis of metamorphic rocks using high-resolution computed X-ray tomography: Part II. Application to natural samples. *Journal of Metamorphic Geology*, **15,** 45–57.

Denison, C., Carlson, W. D. & Ketcham, R. A., 1997. Three-dimensional quantitative textural analysis of metamorphic rocks using high-resolution computed X-ray tomography: Part I. Methods and techniques. *Journal of Metamorphic Geology*, **15,** 29–44.

Dhuime, B., Bosch, D., Bodinier, J. L. *et al.*, 2007. Multistage evolution of the Jijal ultramafic-mafic complex (Kohistan, N Pakistan): implications for building the roots of island arcs. *Earth and Planetary Science Letters*, **261,** 179–200.

Donaldson, C. H., 1976. Experimental investigation of olivine morphology. *Contributions to Mineralogy and Petrology*, **57,** 187–213.

Dornbush, H. J., Weber, K. & Skrotzki, W., 1994. Development of microstructure and texture in high-temperature mylonites from the Ivrea Zone. In: *Textures of Geological Materials* (eds Burg, J. P., Siegesmund, D., Skrotzki, W. & Weber, K.), pp. 187–201. DGM Informationsgesellschaft, Oberursel.

Faure, F., Trolliard, G., Nicollet, C. & Montel, J.-M., 2003. A developmental model of olivine morphology as a function of the cooling rate and the degree of undercooling. *Contributions to Mineralogy and Petrology*, **145,** 251–263.

Fichaut, M., Marcelot, G. & Clocchiatti, R., 1989. Magmatology of Mt. Pelée (Martinique, F.W.I). II: Petrology of gabbroic and dioritic cumulates. *Journal of Volcanology and Geothermal Research*, **38,** 171–187.

Figlarz, M., Gérand, B., Delahaye-Vidal, A., Dumont, B., Harb, F. & Coucou, A., 1990. Topotaxy, nucleation and growth. *Solid State Ionics*, **43,** 143–170.

Garrido, C. J., Bodinier, J. L., Burg, J. P. *et al*., 2006. Petrogenesis of mafic garnet granulite in the lower crust of the Kohistan paleo-arc complex (northern Pakistan): implications for intra-crustal differentiation of island arcs and generation of continental crust. *Journal of Petrology*, **47,** 1873–1914.

Garrido, C. J., Bodinier, J.-L., Dhuime, B. *et al*., 2007. Origin of the island arc Moho transition zone via melt-rock reaction and its implications for intracrustal differentiation of island arcs: evidence from the Jijal complex (Kohistan complex, northern Pakistan). *Geology*, **35,** 683–686.

Hartman, P. & Perdok, W. G., 1955. On the relations between structure and morphology of crystals. *Acta Crystallographica*, **8,** 49–52.

Hibiya, T. & Görnert, P., 2007. Liquid phase epitaxy of garnets. In: *Liquid Phase Epitaxy of Electronic, Optical and Optoelectronic Materials* (eds Capper, P. & Mauk, M.), pp. 305–337. John Wiley & Sons, London.

Hirsch, D. M., Prior, D. J. & Carlson, W. D., 2003. An overgrowth model to explain multiple, dispersed high-Mn regions in the cores of garnet porphyroblasts. *American Mineralogist*, **88,** 131–141.

Holland, T. J. B. & Powell, R., 1998. An internally consistent thermodynamic data set for phases of petrological interest. *Journal of Metamorphic Geology*, **16,** 309–343.

Jamtveit, B. & Andersen, T. B., 1992. Morphological instabilities during rapid growth of metamorphic garnets. *Physics and Chemistry of Minerals*, **19,** 176–184.

Jan, M. Q., 1979. Petrography of the Jijal Complex, Kohistan. In: *Geology of Kohistan, Karakoram Himalaya, Northern Pakistan* (eds Tahirkheli, R. A. K. & Jan, M. Q.), pp. 31–49. University of Peshawar, Peshawar.

Jan, M. Q. & Howie, R. A., 1981. The mineralogy and geochemistry of the metamorphosed basic and ultrabasic rocks of the Jijal Complex, Kohistan, NW Pakistan. *Journal of Petrology*, **22,** 85–126.

Johannes, W. & Koepke, J., 2001. Incomplete reaction of plagioclase in experimental dehydration melting of amphibolite. *Australian Journal of Earth Sciences*, **48,** 581–590.

Ketcham, R. A., 2005. Three-dimensional grain fabric measurements using high-resolution X-ray computed tomography. *Journal of Structural Geology*, **27,** 1217–1228.

Kirkpatrick, R. J., 1981. Kinetics of crystallization of igneous rocks. In: *Kinetics of Geochemical Processes* (eds Lasaga, A. C. & Kirkpatrrick, R. J.), pp. 321–398. Mineralogical Society of America, Washington, DC.

Kleinschrodt, R. & Duyster, J. P., 2002. HT-deformation of garnet: an EBSD study on granulites from Sri Lanka, India and the Ivrea Zone. *Journal of Structural Geology*, **24,** 1829–1844.

Kleinschrodt, R. & McGrew, A., 2000. Garnet plasticity in the lower continental crust: implications for deformation mechanisms based on microstructures and SEM-electron channeling pattern analysis. *Journal of Structural Geology*, **22,** 795–809.

Kretz, R., 1969. On the spatial distribution of crystals in rocks. *Lithos*, **2,** 39–65.

Kretz, R., 1983. Symbols for rock-forming minerals. *American Mineralogist*, **68,** 277–279.

Kuroda, T., Irisawa, T. & Ookawa, A., 1987. Transition from polyhedral to dendritic morphology. In: *Morphology of Crystals* (ed. Sunagawa, I.), pp. 589–612. Terra Scientific Publishing, Tokyo.

Lamoureux, G., Ildefonse, B. & Mainprice, D., 1999. Modelling the seismic properties of fast-spreading ridge crustal Low-Velocity Zones: insights from Oman gabbro textures. *Tectonophysics*, **312,** 283–301.

Lasaga, A. C., 1998. *Kinetic Theory in Earth Sciences*. Princeton University Press, Princeton, NJ.

Mainprice, D., 1990. A FORTRAN program to calculate seismic anisotropy from the lattice preferred orientation of minerals. *Computers & Geosciences*, **16,** 385–393.

Mainprice, D., 2008. ftp://www.gm.univ-montp2.fr/mainprice//CareWare_Unicef_Programs/ date of last access 31 July 2008.

Mainprice, D. & Humbert, M., 1994. Methods of calculating petrophysical properties from lattice preferred orientation data. *Surveys in Geophysics*, **15,** 575–592.

Mainprice, D. & Silver, P. G., 1993. Interpretation of SKS-waves using samples from the subcontinental lithosphere. *Physics of The Earth and Planetary Interiors*, **78,** 257–280.

Mainprice, D., Bascou, J., Cordier, P. & Tommasi, A., 2004. Crystal preferred orientations of garnet: comparison between numerical simulations and electron back-scattered diffraction (EBSD) measurements in naturally deformed eclogites. *Journal of Structural Geology*, **26,** 2089–2102.

Markov, I., 1995. *Crystal Growth for Beginners. Fundamentals of Nucleation, Crystal Growth and Epitaxy*. World Scientific, Singapore.

Markov, I. & Stoyanov, S., 1987. Mechanisms of epitaxial-growth. *Contemporary Physics*, **28,** 267–320.

McLaren, A. C. & Etheridge, M. A., 1976. A transmission electron microscope study of naturally deformed orthopyroxene. *Contributions to Mineralogy and Petrology*, **57,** 163–177.

Meagher, E. P., 1975. Crystal-structures of pyrope and grossularite at elevated-temperatures. *American Mineralogist*, **60,** 218–228.

Mercier, J. C., 1985. Olivine and pyroxenes. In: *Preferred Orientation in Deformed Metals and Rocks* (ed. Wenk, H. R.), pp. 407–430. Academic Press, Orlando, FL.

Michibayashi, K. & Mainprice, D., 2004. The role of pre-existing mechanical anisotropy on shear zone development within oceanic mantle lithosphere: an example from the Oman ophiolite. *Journal of Petrology*, **45,** 405–414.

Nicolas, A. & Ildefonse, B., 1996. Flow mechanism and viscosity in basaltic magma chambers. *Geophysical Research Letters*, **23,** 2013–2016.

Prigogine, I. & Defay, R., 1954. *Chemical Thermodynamics*. Longmans, London.

Prior, D. J., Wheeler, J., Brenker, F. E., Harte, B. & Matthews, M., 2000. Crystal plasticity of natural garnet: new microstructural evidence. *Geology*, **28,** 1003–1006.

Prior, D. J., Wheeler, J., Peruzzo, L., Spiess, R. & Storey, C., 2002. Some garnet micro structures: an illustration of the potential of orientation maps and misorientation analysis in microstructural studies. *Journal of Structural Geology*, **24,** 999–1011.

Putnis, A., 1992. *Introduction to Mineral Sciences*. Cambridge University Press, New York.

Putnis, A. & Putnis, C. V., 2007. The mechanism of reequilibration of solids in the presence of a fluid phase. *Journal of Solid State Chemistry*, **180,** 1783–1786.

Quon, H. H. & Potvin, A. J., 1972. Growth of single crystal rare-earth garnet films by liquid phase epitaxy. *Materials Research Bulletin*, **7,** 463–472.

Ridley, J., 1985. The effect of reaction enthalpy on the progress of a metamorphic reaction. In: *Metamorphic Reactions Kinetics, Textures and Deformation* (eds Thompson, A. B. & Rubie, D. C.), pp. 80–97. Springer, New York.

Ridley, J. & Thompson, A.B., 1986. The role of mineral kinetics in the development of metamorphic microtextures. In: *Fluid-rock Interactions during Metamorphism* (eds Walther, J.V. & Wood, B.J.), pp. 154–193. Springer, New York.

Robertson, J. M., 1978. Liquid-phase epitaxy of garnets. *Journal of Crystal Growth*, **45,** 233–242.

Rubie, D. C., 1998. Disequilibrum during metamorphism: the role of nucleation kinetics. In: *What Drives Metamorphism and Metamorphic Reactions?* (eds Treloar, P. J. & O'Brien, P. J.), pp. 199–214. Geological Society, London.

Spear, F. S. & Kohn, M. A. 2001. *GTB: Program Geothermobarometry, version 2.1*. (available at: http://ees2.geo.rpi.edu/MetaPetaRen/Frame_software.html).

Spiess, R. & Bell, T. H., 1996. Microstructural controls on sites of metamorphic reaction: A case study of the inter-relationship between deformation and metamorphism. *European Journal of Mineralogy*, **8,** 165–186.

Spiess, R., Peruzzo, L., Prior, D. J. & Wheeler, J., 2001. Development of garnet porphyroblasts by multiple nucleation, coalescence and boundary misorientation-driven rotations. *Journal of Metamorphic Geology*, **19,** 269–290.

Spiess, R., Groppo, C. & Compagnoni, R., 2007. When epitaxy controls garnet growth. *Journal of Metamorphic Geology*, **25,** 439–450.

Spry, A., 1969. *Metamorphic Textures*. Pergamon Press, Oxford.

Storey, C. D. & Prior, D. J., 2005. Plastic deformation and recrystallization of garnet: A mechanism to facilitate diffusion creep. *Journal of Petrology*, **46,** 2593–2613.

Sunagawa, I., 1987. Morphology of minerals. In: *Morphology of Crystals* (ed. Sunagawa, I.), pp. 509–587. Terra Scientific Publishing, Tokyo.

Terry, M. P. & Heidelbach, F., 2006. Deformation-enhanced metamorphic reactions and the rheology of high-pressure shear zones, Western Gneiss Region, Norway. *Journal of Metamorphic Geology*, **24,** 3–18.

Thompson, J. B. J., 1978. Biopyriboles and polysomatic series. *American Mineralogist*, **63,** 239–249.

Veblen, D. R., 1991. Polysomatism and polysomatic series – a review and applications. *American Mineralogist*, **76,** 801–826.

Veblen, D. R., 1992. Electron microscopy applied to nonstoichiometry, polysomatism, and replacement reactions in minerals. In: *Reviews in Mineralogy* (ed. Buseck, P. R.), pp. 181–230. Mineralogical Society of America, Washington, DC.

Vollmer, F. W., 1990. An application of eigenvalue methods to structural domain analysis. *Geological Society of America Bulletin*, **102,** 786–791.

Walther, J. V. & Wood, B. J., 1984. Rate and mechanism in prograde metamorphism. *Contributions to Mineralogy and Petrology*, **88,** 246–259.

Waters, D. J. & Lovegrove, D. P., 2002. Assessing the extent of disequilibrium and overstepping of prograde metamorphic reactions in metapelites from the Bushveld Complex aureole, South Africa. *Journal of Metamorphic Geology*, **20,** 135–149.

Whitney, D. L., Goergen, E. T., Ketcham, R. A. & Kunze, K., 2008. Formation of garnet polycrystals during metamorphic crystallization. *Journal of Metamorphic Geology*, **26,** 365–383.

Wilbur, D. E. & Ague, J. J., 2006. Chemical disequilibrium during garnet growth: Monte Carlo simulations of natural crystal morphologies. *Geology*, **34,** 689–692.

Woodcock, N. H. & Naylor, M. A., 1983. Randomness testing in three-dimensional orientation data. *Journal of Structural Geology*, **5,** 539–548.

Worden, R. H., Champness, P. E. & Droop, G. T. R., 1987. Transmission electron-microscopy of the pyrometamorphic breakdown of phengite and chlorite. *Mineralogical Magazine*, **51,** 107–121.

Yamamoto, H., 1993. Contrasting metamorphic *P–T*-time paths of the Kohistan granulites and tectonics of the western Himalayas. *Journal of the Geological Society of London*, **150,** 843–856.

Yamamoto, H. & Yoshino, T., 1998. Superposition of replacements in the mafic granulites of the Jijal complex of the Kohistan arc, northen Pakistan: dehydration and rehydration within deep arc crust. *Lithos*, **43,** 219–234.

Yoshino, T. & Okudaira, T., 2004. Crustal growth by magmatic accretion constrained by metamorphic P–T paths and thermal models of the Kohistan Arc, NW Himalayas. *Journal of Petrology*, **45,** 2287–2302, doi:2210.1093/petrology/egh2056.

Yoshino, T., Yamamoto, H., Okudaira, T. & Toriumi, M., 1998. Crustal thickening of the lower crust of the Kohistan arc (N. Pakistan) deduced from Al zoning in clinopyroxene and plagioclase. *Journal of Metamorphic Geology*, **16,** 729–748.

Yoshinobu, A. S. & Harper, G. D., 2004. Hypersolidus deformation in the lower crust of the Josephine ophiolite: evidence for kinematic decoupling between the upper and lower oceanic crust. *Journal of Structural Geology*, **26,** 163–175.

Zeilinger, G., 2002. Structural and Geochronological Study of the Lowest Kohistan Complex, Indus Kohistan Region in Pakistan, NW Himalaya. PhD Thesis, ETH, Zurich.

Received 8 April 2008; revision accepted 7 July 2008.